

# Numerical Simulations of the Ross Sea Tides

DOUGLAS REED MACAYEAL<sup>1</sup>

*Geophysical Fluid Dynamics Program, Princeton University*

Tidal currents below the floating Ross Ice shelf are reconstructed by using a numerical tidal model. They are predominantly diurnal, achieve maximum strength in regions near where the ice shelf runs aground, and are significantly enhanced by topographic Rossby wave propagation along the ice front. A comparison with observations of the vertical motion of the ice shelf surface indicates that the model reproduces the diurnal tidal characteristics within 20%. Similar agreement for the relatively weak semi-diurnal tides was not obtained, and this calls attention to possible errors of the open boundary forcing obtained from global-ocean tidal simulations and to possible errors in mapping zones of ice shelf grounding. Air-sea contact below the ice shelf is eliminated by the thick ice cover. The dominant sub-ice-shelf circulation may thus be tidally induced. A preliminary assessment of sub-ice-shelf conditions based on the numerical tidal simulations suggests that (1) strong barotropic circulation is driven along the ice front and (2) tidal fronts may form in the sub-ice-shelf cavity where the water column is thin and where the buoyancy input is weak.

## INTRODUCTION

Tidal currents are the strongest observed form of seawater motion in the cavity below the floating ice shelf in the southern Ross Sea [Williams and Robinson, 1979, 1980; Jacobs and Haines, 1982]. The thick ice platform shown in Figure 1 eliminates air-sea contact; thus sub-ice-shelf ocean circulation and heat transport may be forced primarily by tidal currents or by related processes such as tidal current rectification and tidal front formation [MacAyeal, 1983]. Given present ice flow patterns, approximately 25% of the snow that accumulates over Antarctica flows through the Ross Ice Shelf and ablates into the Ross Sea by basal melting or by iceberg calving [Hughes, 1975]. The Ross Sea tidal regime may thus provide a direct and influential link between the ocean and the earth's largest ice mass. This paper presents the results of numerical tidal simulations undertaken to reconstruct the Ross Sea tidal currents and to estimate their influence throughout the sub-ice-shelf cavity.

The Ross Ice Shelf is an integrated ice mass that is flexible when deformed over large horizontal length scales such as those imposed by tides in the water below. As a result of its slow horizontal movement, the ice shelf has provided a natural platform upon which the tidal amplitude and phase have been measured (the 10 observation stations are shown in Figure 2) [Williams and Robinson, 1979, 1980; Williams, 1976, 1979; Thiel, 1960; Thiel et al., 1960]. These measurements show that the diurnal tide is stronger than the semidiurnal tide and that the tidal amplitudes are largest in areas near where the ice shelf runs aground.

In contrast with the tidal amplitude and phase, tidal currents and their effect on the sub-ice-shelf water column have not been measured reliably because of the thick and impenetrable ice cover. The few available tidal current measurements come from north of the ice front (McM and "current meter" in Figure 2) [Heath, 1977; Gilmour et al., 1962; Jacobs and Haines, 1982] and from a single sub-ice-shelf location (J9

in Figure 2), where a bore hole was opened for several days [Clough and Hansen, 1979; Jacobs and Haines, 1982].

Tidal currents can be difficult to reconstruct on the basis of observed tidal amplitude and phase alone because of complex basin shape and topography [Williams, 1976]; hence, the scarcity of reliable tidal current measurements presents a serious obstacle to the investigation of sub-ice-shelf oceanography. Basin topography, for example, may exert a particularly influential control on the currents because, in polar latitudes, topographic Rossby waves can be excited by the diurnal tide. These waves are commonly observed in the Arctic along continental slopes and above isolated seabed bumps [Cartwright, 1969; Huthnance, 1974, 1981; Cartwright et al., 1980; Thomson and Crawford, 1982]. It is therefore reasonable to expect such waves along sections of the ice front, along various seabed ridges below the ice shelf, and along the continental slope north of the Ross Sea. As a result of their strong currents, these waves could induce significant stirring in the sub-ice-shelf environment. Current meter records, however, are generally required to detect topographic Rossby waves [Cartwright, 1969]; thus, to detect them below the ice shelf, the available observations of tidal amplitude and phase must be coordinated with numerical simulations capable of accurately reconstructing the tidal currents.

The numerical tidal simulations conducted in this study are intended to amplify the existing observations by calculating the sub-ice-shelf tidal currents and by extending the maps of tidal amplitude and phase across regions not covered by the data collection network.

## MODEL EQUATIONS AND PROCEDURE

The governing equations for barotropic tidal motion employed in this study are [Nihoul, 1975, p. 51]

$$\partial(\mathbf{Du})/\partial t + \nabla \cdot (D\mathbf{uu}) = -gD\nabla(\eta - \eta_e) - fD\mathbf{e}_z \times \mathbf{u} - k|\mathbf{u}|\mathbf{u} + \nu D\nabla^2 \mathbf{u} \quad (1)$$

and

$$\partial\eta/\partial t + \nabla \cdot (D\mathbf{u}) = 0 \quad (2)$$

where  $\mathbf{u}$  is the depth-averaged horizontal velocity,  $\eta$  is the departure of the sea surface or ice shelf base from the level of rest,  $D$  is the instantaneous depth of the water layer (extending from the seabed to either the sea surface or the ice shelf base),

<sup>1</sup>Now at Department of the Geophysical Sciences, The University of Chicago.

Copyright 1984 by the American Geophysical Union.

Paper number 3C1414.  
0148-0227/84/003C-1414\$05.00

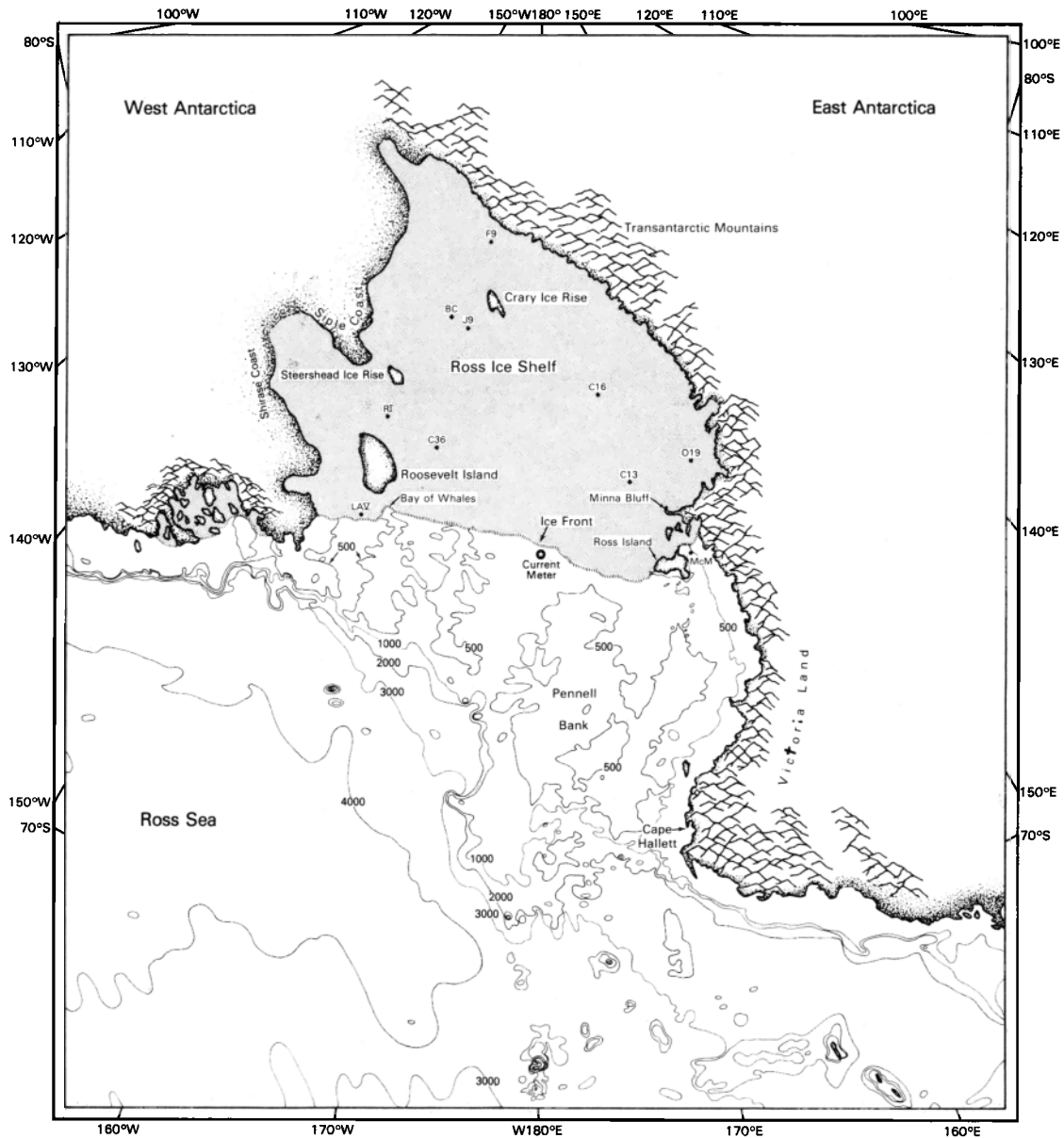


Fig. 1. At the margins of the West Antarctic Ice Sheet, large floating ice shelves (indicated by shading) extend seaward from where the ice floats free of the seabed. The Ross Ice Shelf, shown above, occupies the southern half of the Ross Sea. It ranges in thickness from 1100 to 100 m, covers an area of 580,000 km<sup>2</sup>, and flows toward the open ocean at rates of up to 1200 m/yr. Air-sea contact is prohibited within the sub-ice-shelf cavity; hence, tidal currents and related tidally driven processes may contribute to ocean circulation below the ice shelf and associated basal-ice ablation. Although observations of the tidal amplitudes and phases have been made at 10 locations distributed across the ice shelf covered portion of the Ross Sea (indicated above by dots) [Williams and Robinson, 1979, 1980], this paper presents the results of numerical tidal simulations conducted to investigate the sub-ice-shelf tidal currents. This map is traced from the polar-stereographic projection of the *American Geographical Society of New York* [1970].

$\eta_e$  is the equilibrium tidal elevation specifying forcing by the sun and moon [Dietrich, 1963, p. 443],  $g = 9.81 \text{ m/s}^2$  is the gravitational acceleration,  $f = -1.42 \times 10^{-4} \text{ s}^{-1}$  is the Coriolis parameter at the mean latitude of the Ross Sea (78°S),  $k$  is the nondimensional quadratic bottom-friction parameter equal to  $2.5 \times 10^{-3}$  in open water and  $5.0 \times 10^{-3}$  in ice shelf covered water [Rämming and Kowalik, 1980, p. 17],  $\nu = 100 \text{ m}^2/\text{s}$  is the eddy viscosity (selected arbitrarily to suppress numerical noise, but otherwise of small importance), and  $\mathbf{e}_z$  is a unit vector that is perpendicular to the geoid.

The elastic strength of the ice shelf and its inertia with respect to vertical motion are disregarded in this study for simplification. Although ice shelf tidal flexure may provide a

significant influence within several kilometers of coasts [Hughes, 1977; Holdsworth, 1977; MacAyeal, 1983], its effect on tidal propagation through the central part of the basin is thought to be minor [Williams and Robinson, 1981].

Boundary conditions applied at coasts are  $\mathbf{u} \cdot \mathbf{e}_n = 0$ , where  $\mathbf{e}_n$  is the outward pointing unit vector that is perpendicular to the coast and  $\partial(\mathbf{u} \cdot \mathbf{e}_t)/\partial n + (2/\Delta x)\mathbf{u} \cdot \mathbf{e}_t = 0$ , where  $\mathbf{e}_t$  is the unit vector tangent to the coast,  $\partial(\mathbf{u} \cdot \mathbf{e}_t)/\partial n$  is the gradient of the longshore flow in the direction of  $\mathbf{e}_n$ , and  $\Delta x$  is the finite difference grid point spacing (10 km). The first condition listed above represents the no cross-shore flux condition, and the second condition listed above represents a computationally efficient compromise between the no-slip and free-slip con-

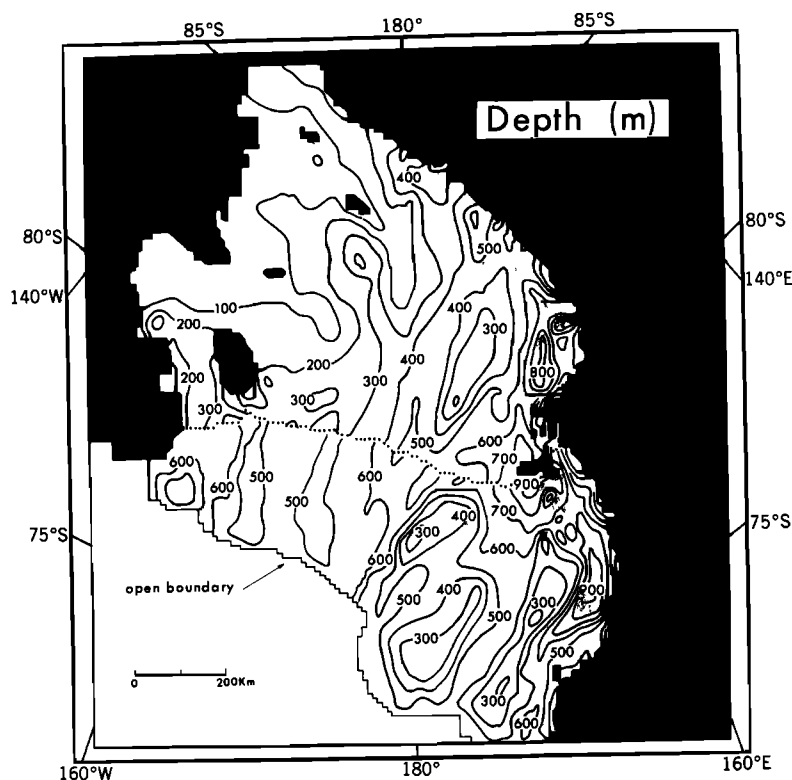


Fig. 2. The numerical domain is bounded by the mountainous coasts, the ice shelf grounding line, and the open boundary. Depth in the open portion of the Ross Sea is obtained from Hayes and Davey [1974]. South of the ice front (indicated by the dotted line transecting the basin from the east to the west), the water depth is defined as the thickness of the seawater layer alone and is obtained from Greischar and Bentley [1980].

ditions associated with the eddy viscosity term in equation (1). This second condition produces no noticeable effect on the model simulation.

Tidal forcing is accomplished by specifying the astronomic tide-generating potential,  $\eta_e$ , and by specifying the sea-surface elevation,  $\eta$ , as a function of time and position along the open boundary shown in Figure 2. The open boundary conditions are the strongest form of forcing and were obtained from Schwiderski's [1980b, 1981a, b, c, d, e] global-ocean simulations of the diurnal and semidiurnal tides. Direct observations of tidal conditions along the open boundary do not exist; hence, Schwiderski's data, accurate to within 0.05 m of amplitude and 15° of phase [Schwiderski, 1980a], represent the best available source of model forcing data. Preliminary numerical simulations encompassing minor alterations of the open boundary conditions, in an attempt to reproduce better the observed tidal fields, proved to be unsuccessful and computationally expensive; therefore, further improvement of the open boundary forcing by a trial-and-error process was not attempted.

TABLE 1. Tidal Constants

Symbol	Name	Species	Frequency, $10^{-4} \text{ s}^{-1}$
K1	declinational luni-solar	diurnal	0.72921
O1	principal lunar	diurnal	0.67598
P1	principal solar	diurnal	0.72523
M2	principal lunar	semidiurnal	1.40519
S2	principal solar	semidiurnal	1.45444
N2	elliptical lunar	semidiurnal	1.37880

From Dietrich [1963, pp. 426-427].

Two additional conditions applied at the open boundary are  $\nabla \cdot (Duu) = 0$  and  $vDV^2u = 0$ . These conditions represent suppression of the momentum flux convergence and the viscous drag at the open boundary where information required to compute these terms must otherwise come from outside the model domain. Outward wave radiation through the open boundary, such as that described by Blumberg and Kantha [1982], was not accommodated explicitly in this study. As a result, small-scale high-frequency waves introduced during the model spin-up period were artificially reflected at the open boundary. These waves were damped during model spin-up by raising the eddy viscosity.

The finite difference grid representing the Ross Sea consists of a  $110 \times 160$  rectangular array of grid points with 10 km spacing. This grid spacing is approximately the same as the horizontal range of water parcel movement during the diurnal tidal cycle and is therefore advantageous for simulation of such processes as tidal current rectification [Zimmerman, 1981]. Map magnification factors adjusting for the polar stereographic projection of the earth's surface were disregarded [Kowalik and Untersteiner, 1978]. Topography of the model domain, displayed in Figure 2, was constructed from maps compiled by Hayes and Davey [1974], by Greischar and Bentley [1980], and by Rose [1979]. The open boundary lies along the 600 m depth contour at the northern margin of the continental shelf. The topography near the open boundary was smoothed, and some sections were straightened to suppress numerical noise.

The finite-difference forms of equations (1) and (2), and the boundary conditions used in this study, are essentially the same as those used by L. Y. Oey and G. L. Mellor (unpub-

TABLE 2. Comparison of the Simulated (S) and the Observed (O) Tidal Amplitude and Phase at 10 Ross Sea Locations Shown in Figure (2)

Station	Amplitude, 10 <sup>-2</sup> m											
	K1		O1		P1		M2		S2		N2	
	S	O	S	O	S	O	S	O	S	O	S	O
LAV	41	34	32	25	14	11	9	3	6	5	4	5
McM	28	26	22	26	9	9	8	4	8	2	4	3
C13	35	30	27	34	11	10	7	3	7	4	3	9
O19	37	31	28	29	12	10	8	4	8	2	3	3
C36	45	37	35	32	15	12	8	3	5	6	4	4
RI	55	44	40	38	19	15	15	5	8	10	8	9
J9	50	37	36	37	16	12	4	7	3	8	3	7
C16	38	31	29	27	12	10	6	3	6	2	2	4
BC	54	43	39	35	17	14	7	8	5	10	4	9
F9	57	41	39	40	19	14	16	8	16	11	8	8
Σ S - O /10	8.6		3.2		2.7		4.8		3.8		2.0	

Station	Phase*											
	K1		O1		P1		M2		S2		N2	
	S	O	S	O	S	O	S	O	S	O	S	O
LAV	156	154	141	141	155	154	162	35	299	342	267	344
McM	229	196	204	186	228	196	147	6	307	268	264	234
C13	219	200	198	190	218	200	136	300	280	130	252	160
O19	224	208	202	196	222	208	128	340	271	190	241	185
C36	175	160	158	153	176	160	187	75	316	25	300	44
RI	162	160	145	140	162	160	209	130	333	26	322	5
J9	194	191	178	172	193	191	282	205	112	106	32	78
C16	216	200	196	190	215	200	117	310	249	160	228	147
BC	193	186	176	174	192	186	290	213	100	112	39	94
F9	213	206	193	190	209	206	13	258	160	142	118	168
Σ S - O /10	12		6		11		121		56		62	

\*Degrees with respect to the Greenwich meridian.

lished manuscript, 1982), so will not be described here. Simulations of each of the three diurnal and three semidiurnal tides listed in Table 1 were begun from a state of rest, run through five tidal cycles to allow spin-up, and then Fourier analyzed on the sixth cycle to obtain the relevant tidal fields. Allowing additional warm-up cycles before analysis did not alter the results by more than 5%.

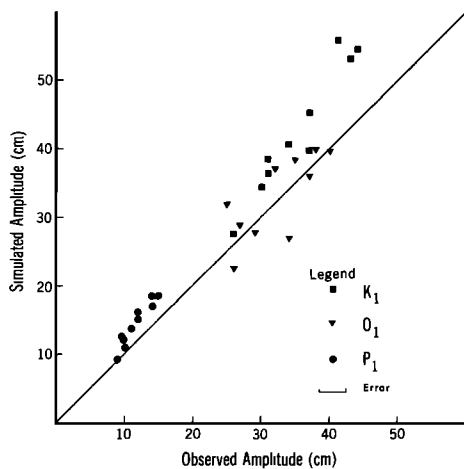


Fig. 3. The simulated and observed amplitude of the three diurnal tides at the 10 tidal measurement stations are compared by plotting points on a graph having the observed and the simulated amplitudes as coordinate axes. Perfect agreement is achieved when points fall on a line extending at a 45° angle from the origin (the thin line).

EVALUATION OF MODEL PERFORMANCE

The tidal simulations are compared with the observations obtained by Williams and Robinson [1979, 1980] in Table 2 and in Figures 3 and 4. The diurnal tidal simulations achieved the best agreement with the observations. This is encouraging because the diurnal tides dominate the Ross Sea tidal regime and are, therefore, more likely to control the oceanographic conditions below the ice shelf. Figure 3 indicates that the simulated diurnal amplitudes are approximately 20% higher than

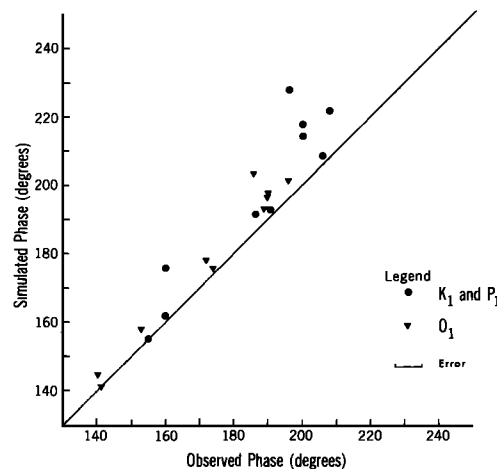


Fig. 4. The simulated and observed phase of the three diurnal tides at the 10 tidal measurement stations are compared in this diagram.

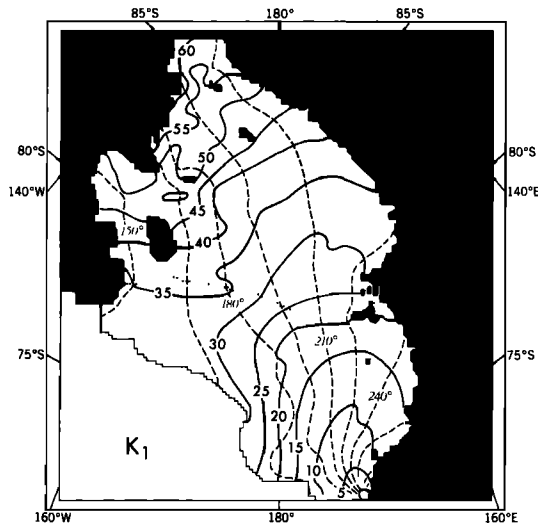


Fig. 5. The simulated K1 amplitude is contoured (solid lines) in centimeters, and the simulated K1 phase is contoured (broken lines) in degrees relative to Greenwich. The other two simulated diurnal tides, O1 and P1, displayed patterns similar to those above.

the observed diurnal amplitudes. The anticipated uncertainty of the open boundary forcing [Schwiderski, 1980a], coupled with the tendency toward tidal amplification south of the open boundary (see Figure 5), may account for this disagreement. Although corrections of the boundary conditions could have been incorporated, a trial-and-error adjustment was rejected because of its potential expense.

Disagreement between the simulated and observed semi-diurnal tidal fields was substantially greater than that between the simulated and observed diurnal tides (Table 2). The simulated M2 tide shown in Figure 6, for example, consists of an amphidromic regime occupying the ice shelf-covered portion of the basin. This pattern agrees with the observed pattern [mapped in Figure 6 of Williams and Robinson, 1980], with the exception of three discrepancies: the simulated phase is shifted by approximately  $180^\circ$  from the observed phase (see Figure 6), the simulated amphidromic point is shifted approximately 150 km toward the southeast, and the simulated amplitude displays greater amplification along the Siple Coast.

The phase error of the simulated semi-diurnal tide may be attributed to the open boundary forcing. Williams and Robinson [1980] noticed a similar discrepancy between their data and global ocean tidal model simulations available at the time of their study. This led them to construct two alternative maps of the M2 phase contours (compare their Figures 6 and 9). One of these alternatives is qualitatively similar to that presented in Figure 6, but the other displays a virtual amphidromic point [Schwiderski, 1980a] residing inland from the Shirase Coast.

Mislocation of the simulated semi-diurnal amphidromic point and overamplification along the Siple Coast may result from errors in the specified locations of ice shelf grounding or from the effects of ice shelf flexure disregarded in equation (1). Thomas and Bentley [1978] and K. C. Jezek (unpublished manuscript, 1982), report several areas of ice shelf grounding along the Siple Coast southeast of Cray Ice Rise. These grounded regions are not represented in the model domain; thus, their influence could be responsible for significant model error. The effects of ice shelf rigidity and of the ice shelf's inertia during tidal rise and fall may additionally distort the

simulated semi-diurnal tidal fields along the Siple Coast. These effects are expected to be most pronounced for the semi-diurnal tides because the sea surface curvature is generally larger than that of the diurnal tide and because the frequency is relatively high.

#### INTERPRETATION OF SIMULATED AMPLITUDE AND PHASE

The characteristics of the simulated amplitude and phase, shown for two representative tides K1 and M2 in Figures 5 and 6, respectively, may be explained in terms of Kelvin wave dynamics [Gill, 1982, p. 378]. Both the diurnal and semi-diurnal amphidromic points, for example, constitute destructive interference produced by Kelvin wave propagation about the curved coastline of the Ross Sea. By using the basin-averaged depth of 400 m, the wavelengths of diurnal and semi-diurnal Kelvin waves are 5400 and 2700 km, respectively. The length of the curved Ross Sea coastline, from its eastern point on the Shirase Coast to Cape Hallett, is approximately 3000 km. The Ross Sea will thus contain a single wavelength of the semi-diurnal Kelvin wave. In this circumstance, the semi-diurnal tide along the eastern and western sides of the basin will be  $180^\circ$  out of phase, and destructive interference will occur in the basin's center. Such an interference pattern is consistent with the central amphidromic point of M2 displayed in Figure 6.

The diurnal amphidromic point off Cape Hallett results from interference between a deep-ocean tidal wave propagating directly across the mouth of the Ross Sea and the coastal Kelvin wave that propagates along the interior coastline of the shallow basin. The 5400-km wavelength of the interior Kelvin wave results in a  $200^\circ$  phase lag between the eastern margin of the Ross Sea and Cape Hallett. Assuming that the wavelength of the deep-ocean tide is equal to the circumference of Antarc-

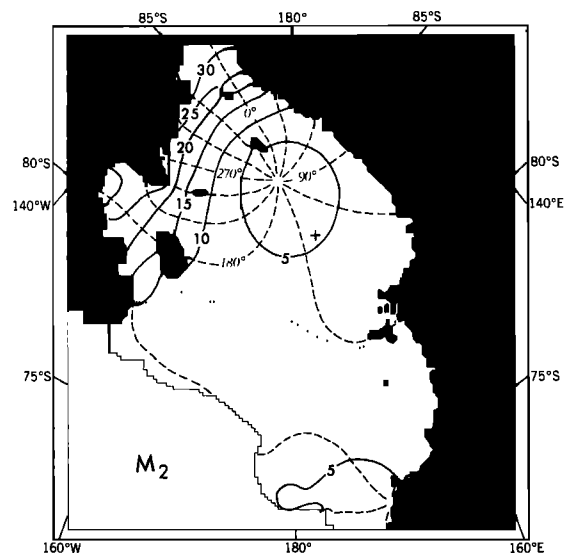


Fig. 6. The simulated M2 tidal amplitude is contoured (solid lines) in centimeters, and the simulated M2 phase is contoured (broken lines) in degrees relative to Greenwich. The other two simulated semi-diurnal tides, S2 and N2, displayed patterns similar to those above. A cross northwest of the central M2 amphidromic point indicates one of the two alternative locations where Williams and Robinson [1980] have mapped an M2 amphidromic point from their data. For this alternative, the observed  $0^\circ$  phase contour (not shown) extends from this cross toward Minna Bluff (Figure 1). The other alternative map presented by Williams and Robinson [1980] exhibits a virtual amphidromic point inland from the Shirase Coast.

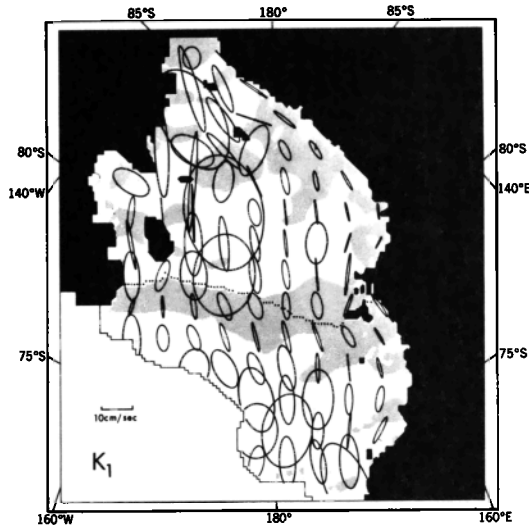


Fig. 7. The imaginary figure traced by the tidal current vector at a particular location during a complete tidal cycle is called the tidal current ellipse. The simulated K1 tidal current ellipses shown above are drawn at every tenth grid point above. Shading denotes regions where the tidal current vectors rotate clockwise rather than counter-clockwise. The K1 tidal currents exhibit a strip of clockwise rotation just seaward of the ice front resulting from topographic Rossby wave propagation along the ice front. Over most of the basin, the K1 tidal current ellipses are oriented north-south. This feature accompanies a geostrophic balance between the tidal currents and the sea surface elevation gradient.

tica [Schwiderski, 1981b], the deep-ocean tide will exhibit a 20° phase lag between the same two points. If the two waves are in phase at the eastern margin of the Ross Sea, then the two waves will be 180° out of phase off Cape Hallett, and destructive interference will result.

Intensification of the diurnal and semidiurnal amplitudes along the shallow Siple Coast may also be related to coastal Kelvin wave dynamics. In an ocean of constant depth, a

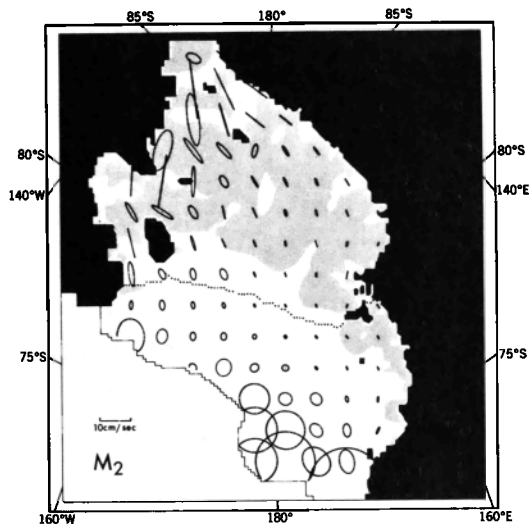


Fig. 8. The simulated M2 tidal current ellipses south of the ice front tend to be oriented along the direction of the nearest coastline and are very narrow. This is consistent with the dynamics of a coastal Kelvin wave propagating about the curved coastline of the basin as suggested by the M2 amplitude and phase distributions shown in Figure 6. Near the northern margin of the Ross Sea, the simulated M2 tidal current ellipses indicate a balance between the acceleration and the Coriolis force.

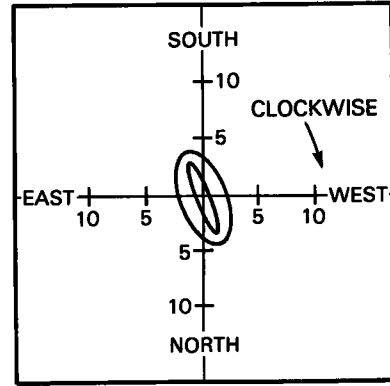


Fig. 9. Jacobs [in Jacobs and Haines, 1982] obtained a 7-month current meter record from the position labeled "current meter" in Figure 1. The observed K1 tidal current ellipse given by this record is smaller than that of the simulation. Both ellipses, however, have clockwise polarization. Axis labels are in units of centimeters per second.

Kelvin wave attains its maximum amplitude at the coast and exhibits exponential offshore decay, with an  $e$  folding decay scale equal to the Rossby radius of deformation,  $(gD/f^2)^{1/2}$  [Gill, 1982, p. 379]. In the vicinity of the Siple Coast, the offshore decay scale displayed by the semidiurnal tide is approximately 220 km and is consistent with the Rossby radius of deformation determined from the local depth. The diurnal tide is not as sensitive to the shallow depth along the Siple Coast and, therefore, exhibits more gentle offshore decay.

SIMULATED TIDAL CURRENTS

The tidal current ellipse is the imaginary figure traced out by a tidal current vector during a complete tidal cycle. The

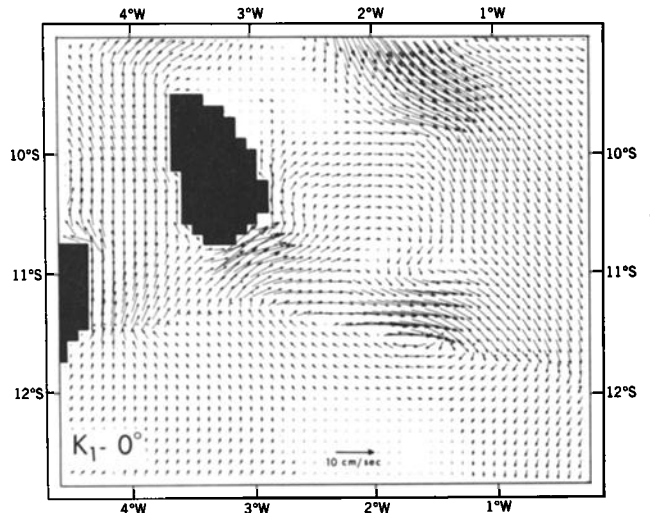


Fig. 10. The K1 tidal currents at 0° phase (180° phase may be obtained by reversing the direction of the vectors pictured here) along the eastern end of the ice front are unusually strong and display high cross ice front shear. These features are manifestations of topographic Rossby wave propagation along the discontinuity of depth found at the ice front. The false latitude and longitude coordinates indicated at the outside margins of this map represent a grid coordinate system in which the intersection of the prime meridian and the equator is defined to be North Pole. This coordinate system has been adopted, by agreement among investigators, for presentation of Ross Ice Shelf field data. All directions referenced in the text, however, are specified relative to the true directions. The island in the top left of this figure is Roosevelt Island.

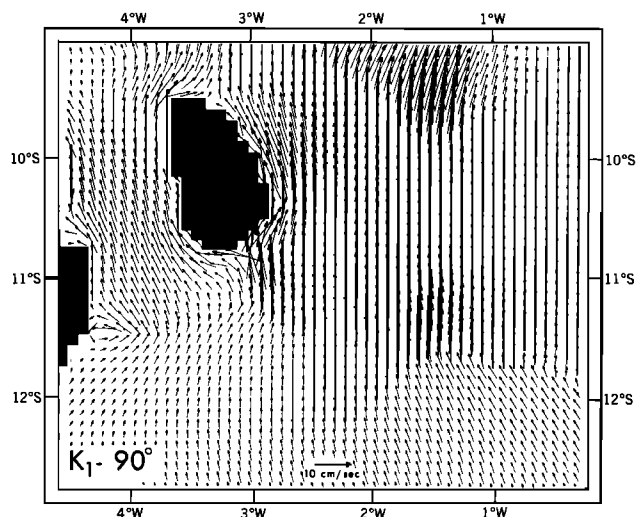


Fig. 11. The K1 tidal currents at 90° phase along the eastern end of the ice front are nearly in geostrophic balance with the free surface slope (Figure 5). The strong cross ice front shear occurring at 0° phase (in Figure 10) northwest of Roosevelt Island has reduced, but another such feature now occurs at the junction of the ice front with the Shirase Coast.

polarization of this ellipse is either clockwise or counterclockwise. Figures 7 and 8 display the simulated tidal current ellipses of K1 and M2 at select locations throughout the Ross Sea. The shaded regions of Figures 7 and 8 are where clockwise polarization occurs. Figure 9 presents a comparison between the simulated and the observed K1 tidal-current ellipse at the ice front position labeled "current meter" in Figure 1. Although the orientation and polarization of the simulated and observed K1 tidal current ellipses agree, the simulated current is stronger by approximately 20%.

The two most distinctive features of the simulated K1 tidal-current ellipses are (1) the strip of anomalous clockwise polarization aligned with the ice front and (2) the north/south orientation of the semi-major axes. The anomalous polarization is related to a special form of topographic Rossby wave that propagates westward along the depth discontinuity embodied by the ice front. This wave is discussed in the next section. The north/south orientation of the K1 ellipses is related to the balance of forces governing the tidal currents. Denoting the westward and southward tidal current components by  $u$  and  $v$ , respectively, the complex ratio  $v/u$  indicates the polarization, orientation, and ellipticity of the tidal current ellipse [Munk *et al.*, 1970]. The simulations indicate that the K1 currents exhibit the following approximate momentum balance:  $\partial v/\partial t + fu = 0$  and  $\partial u/\partial t + g\partial\eta/\partial x = 0$ , where  $\partial\eta/\partial x$  is the gradient of  $\eta$  in the westward direction. This approximate momentum balance indicates that the maximum southward flow is 90° in advance of the maximum free surface elevation and that the southward acceleration is driven by the Coriolis force on the westward flow. The ratio  $v/u$ , in the present circumstance, is  $-if/\omega$ , where  $\omega$  is the K1 frequency. This ratio implies that (1) the semi-major axis of the K1 ellipse is twice as long as the semi-minor axis (because  $f \approx 2\omega$ ), (2) the semi-major axis is oriented north-south, and (3) the polarization is counterclockwise. This last point explains why the strip of clockwise polarization transecting the basin along the ice front is considered unusual.

Over much of the Ross Sea, the M2 tidal currents are rectilinear and are aligned parallel to the nearest coast. These

features are consistent with the Kelvin wave dynamics discussed previously in reference to the M2 amplitude and phase patterns. Near the open boundary, the M2 ellipses are nearly circular and are polarized counterclockwise. These features indicate a balance between the relative acceleration and the Coriolis force. Although this balance can be expected for the semidiurnal tide along the seaward margin of the continental shelf [Munk *et al.*, 1970], these simulated features may also result from numerical noise generated at the open boundary.

#### DIURNAL PERIOD TOPOGRAPHIC ROSSBY WAVES

Topographic Rossby wave excitation was exhibited by the diurnal simulations along some of the shallow seabed ridges extending northwest of the Siple Coast and, most notably, along the eastern segment of the ice front. The K1 flow along the ice front segment, shown in Figures 10 and 11, is unusually strong and displays high cross ice front shear during portions of the tidal cycle. Moreover, the diurnal tidal current ellipse polarization, shown in Figure 7, reverses across the ice front and displays a strip of clockwise polarization that transects the basin along the northern side of the ice front. There is indirect observational evidence in support of the strong currents along the ice front segment shown in Figures 10 and 11. Truesdale and Kellogg [1979], for example, report a low diatom assemblage abundance in this area consistent with strong winnowing of the seabed sediments.

Longuet-Higgins [1968], Rhines [1969], and Chapman [1982], for example, have developed simple analytic treatments for topographic Rossby wave propagation along a discontinuity of depth. Because the ice front manifests itself as a cliff that blocks the upper 200 m of the water column, these previous studies may be applied to explain the results of the simulation. The equation relating frequency to wavelength derived by Rhines [1969] defines the maximum frequency supporting topographic Rossby wave propagation along a given ice front [Longuet-Higgins, 1968]. If  $\omega$  is this upper bound, and  $h_1$  and  $h_2 > h_1$  are the depths on the two sides of the ice front, Rhines' [1969] dispersion relation is written

$$\omega/f = (h_2/h_1 - 1)/(h_2/h_1 + 1) \quad (3)$$

The right-hand side of equation (3) is less than unity; therefore,  $\omega$  must be less than the inertial frequency  $f$ . In polar latitudes, the diurnal tides have a frequency approximately half as large as  $f$  so will excite topographic Rossby waves wherever  $h_2/h_1 > 2$ . The semidiurnal tides, in contrast, have a frequency nearly equal to  $f$  so will not excite topographic Rossby waves along the ice front unless  $h_2/h_1 \gg 1$ . Although  $\omega$  does not depend on the wavelength in Rhines' [1969] analysis, the phase propagation is in the direction having shallow water on the left (in the southern hemisphere).

The value of  $\omega$  defining the maximum frequency for topographic Rossby wave propagation may be computed from equation (3) by using the observed ratio  $h_2/h_1$  (Figure 2). This value exceeds the frequency band of the diurnal tides along two short segments: at the extreme eastern end of the ice front and at a position northwest of Roosevelt Island.

The currents associated with topographic Rossby waves have the following three characteristics [Rhines, 1969]: (1) the current magnitude is maximum at the ice front and decays on either side with an  $e$  folding decay scale equal to the wavelength (approximately 100 km in the simulations); (2) the long ice front flow has opposite directions on either side of the ice front; and (3) the tidal-current ellipses are polarized clockwise

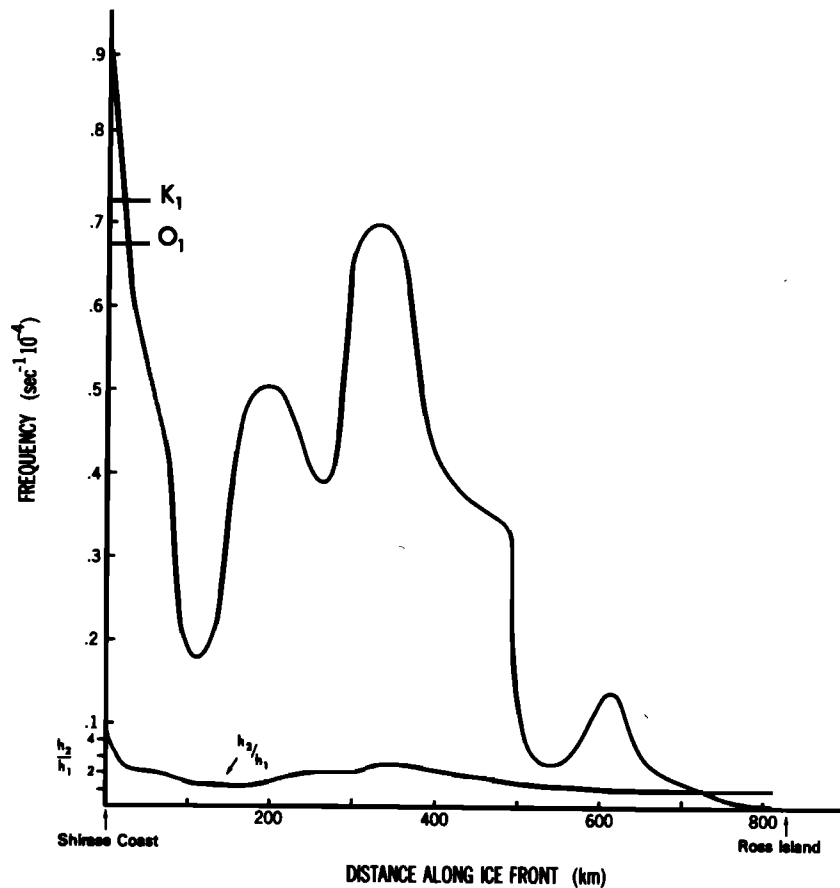


Fig. 12. The strong tidal current shear and the tidal current ellipse polarization reversal at the ice front indicate possible topographic Rossby wave excitation by the diurnal tides. The analysis of Rhines [1969] and Longuet-Higgins [1968] indicates that a maximum frequency cutoff exists, above which such waves cease to propagate. This cutoff is a function of the ratio of the depths on either side of the ice front ( $h_2/h_1$ ) and is plotted above as a function of position along the ice front by using observed depths. The frequencies of the diurnal tides fall below this curve along two segments of the ice front where the  $K_1$  tidal currents displayed in Figures (10) and (11) exhibit strong cross ice front shear.

and counterclockwise on the shallow and deep sides of the ice front, respectively. The simulated diurnal tidal currents are consistent with these traits along the two segments of the ice front where the depth ratio,  $h_2/h_1$ , exceeds 2. The polarization reversal is displayed along the entire ice front, and this suggests that these waves influence the regions beyond the short ice front segments where their propagation is strictly allowed.

#### RESPONSE OF THE SUB-ICE-SHELF CAVITY TO STRONG TIDAL CURRENTS

Preliminary assessment of tidal current rectification and tidal front formation may be accomplished by applying the scales of the simulated tidal currents to simple analytic formulas. Robinson's [1981] treatment of tidal rectification, for example, provides an appropriate order-of-magnitude estimate of the time-independent barotropic circulation driven by tidal currents. His expressions for the magnitude of this circulation,  $\langle u \rangle$ , along a seabed ridge and an ice front are  $\langle u \rangle = 6.3 \times 10^{-3} (\text{m}^{-2} \text{s}^{-1}) \Delta y Y \partial D / \partial y$  and  $\langle u \rangle = 0.11 (\text{m s}^{-1}) \Delta D / D$ , respectively. In these expressions,  $Y$  is the range of cross-isobath water column displacement driven by tidal currents,  $\Delta y$  is the width of the seabed ridge,  $\partial D / \partial y$  is the water depth gradient, and  $\Delta D$  is the depth change across the ice front. Using parameter values representing the seabed ridges extending from the Siple Coast and the ice front northwest of Roosevelt Island, the estimates of  $\langle u \rangle$  are 0.0025 m/s and 0.06 m/s,

respectively. The estimated residual circulation along the ice front is large and could lead to significant cross ice front heat transport [MacAyeal, 1983].

Tidal fronts comprise the boundaries between stratified regions and areas where the water column is vertically well mixed by the action of the tidal currents [Simpson and Pingree, 1977]. A rough estimate of tidal front positions below the Ross Ice Shelf may be accomplished by comparing the rate at which tidal currents dissipate energy by generating small-scale turbulence to the buoyancy flux maintaining stratification [Fearhead, 1975].

Vertically well-mixed conditions are expected along the Siple Coast where ice shelf shoaling reduces the water column thickness below a critical value and where the buoyancy influx is likely to be weak [MacAyeal, 1983]. Hydrographic measurements through the J9 bore hole [Foster, 1983] are consistent with the suspected presence of tidal fronts in the southeastern section of the sub-ice-shelf cavity. Moreover, hydrographic sections along the ice front [Jacobs et al., 1979] reveal glacial meltwater emerging from the sub-ice-shelf cavity at depths in excess of 400 m. Correspondence between this depth and the large ice shelf draft along the Siple Coast suggests that zones of basal melting correlate with zones of strong vertical mixing induced by tidal currents. Tidal currents may thus provide a dominant catalyst for strong vertical heat transfer necessary for basal melting and associated thermohaline circulation.

*Acknowledgments.* I thank the faculty and staff of the Geophysical Fluid Dynamics Program of Princeton University, and of the Oceans and Ice Branch of Goddard Space Flight Center, for valuable scientific assistance, preparation of figures, and computer time. In addition, I thank the many reviewers who helped to improve the quality of this manuscript. This research was supported by the NASA Student Training Program grant NGT 031-001-800, by Princeton University, by the Geophysical Fluid Dynamics Laboratory of NOAA, and by the National Science Foundation grant DPP 81-19863.

## REFERENCES

- American Geographical Society of New York, Antarctica (map, 1:5,000,000; stereographic projection), sheet 13, 1970.
- Blumberg, A. F., and L. H. Kantha, A numerical model of the shelf circulation in the middle Atlantic bight by tides, transient storms and the offshore, large-scale circulation: Formulation of proper open boundary conditions, *Tech. Rep. 73*, Princeton Univ., Princeton, N. J., 1982.
- Cartwright, D. E., Extraordinary tidal currents near St. Kilda, *Nature*, 223, 928-932, 1969.
- Cartwright, D. E., J. M. Huthnance, R. Spencer, and J. M. Vassie, On the St. Kilda shelf tidal regime, *Deep Sea Res.*, 27, 61-70, 1980.
- Chapman, D. C., On the failure of Laplace's tidal equations to model subinertial motions at a discontinuity in depth, *Dyn. Atmos. Oceans*, 7, 1-16, 1982.
- Clough, J. W., and B. L. Hansen, The Ross Ice Shelf Project, *Science*, 203, 433-434, 1979.
- Dietrich, G., *General Oceanography: An Introduction*, Wiley-Interscience, New York, 1963.
- Fearnhead, P. G., On the formation of fronts by tidal mixing around the British Isles, *Deep Sea Res.*, 22, 311-321, 1975.
- Foster, T. D., The temperature and salinity fine structure of the ocean under the Ross Ice Shelf, *J. Geophys. Res.*, 88, 2556-2564, 1983.
- Gill, A. E., *Atmosphere-Ocean Dynamics*, Academic, New York, 1982.
- Gilmour, A. E., W. J. P. MacDonald, and F. G. Van der Hoeven, Winter measurements of sea currents in McMurdo Sound, *N. Z. J. Geol. Geophys.*, 5, 778-789, 1962.
- Greischar, L. L., and C. R. Bentley, Isostatic equilibrium grounding line between the West Antarctic inland ice sheet and the Ross Ice Shelf, *Nature*, 283, 651-654, 1980.
- Hayes, D. E., and F. J. Davey, A geophysical study of the Ross Sea, Antarctica, in *Initial Reports of the DSDP*, vol. 28, edited by D. E. Hayes et al., pp. 263-278, U.S. Government Printing Office, Washington, D.C., 1974.
- Heath, R. A., Circulation across the ice shelf edge in McMurdo Sound, Antarctica, in *Polar Oceans*, edited by M. J. Dunbar, pp. 129-149, Arctic Institute of North America, Calgary, 1977.
- Holdsworth, G., Tidal interaction with ice shelves, *Ann. Geophys.*, 33, 133-146, 1977.
- Hughes, T. J., The West Antarctic ice sheet: Instability, disintegration, and initiation of ice ages, *Rev. Geophys. Space Phys.*, 13, 502-526, 1975.
- Hughes, T. J., West Antarctic ice streams, *Rev. Geophys. Space Phys.*, 15, 1-46, 1977.
- Huthnance, J. M., On the diurnal tidal currents over Rockall Bank, *Deep Sea Res.*, 21, 23-35, 1974.
- Huthnance, J. M., On mass transports generated by tide and long waves, *J. Fluid Mech.*, 102, 367-387, 1981.
- Jacobs, S. S., and W. E. Haines, Oceanographic data in the Ross Sea and along the George V Coast, 1976-1979, *Ross Ice Shelf Proj. Tech. Rep. LDGO-82-1*, Lamont-Doherty Geol. Obs., Palisades, New York, 1982.
- Jacobs, S. S., A. L. Gordon, and J. L. Ardai, Jr. Circulation and melting beneath the Ross ice Shelf, *Science*, 203, 441-443, 1979.
- Kowalik, Z., and N. Untersteiner, A study of the M2 tide in the Arctic Ocean, *Deut. Hydrogr. Zeit.*, 31, 216-229, 1978.
- Longuet-Higgins, M. S., On the trapping of waves along a discontinuity of depth in a rotating ocean, *J. Fluid Mech.*, 31, 417-435, 1968.
- MacAyeal, D. R., Rectified Tidal Currents and Tidal-Mixing Fronts: Controls on the Ross-Ice Shelf Flow and Mass Balance, Ph.D. thesis, Princeton Univ., Princeton, N. J., 1983.
- Munk, W., F. Snodgrass, and M. Wimbush, Tides off-shore: Transition from California coastal to deep-sea waters, *Geophys. Fluid Dyn.*, 1, 161-235, 1970.
- Nihoul, J. C. J., Hydrodynamic models, in *Modelling of Marine Systems, Elsevier Oceanogr. Ser.*, vol. 10, edited by J. C. J. Nihoul, pp. 41-67, Elsevier, New York, 1975.
- Ramming, H. G., and Z. Kowalik, *Numerical Modelling of Marine Hydrodynamics, Applications to Dynamic Physical Processes, Elsevier Oceanogr. Ser.*, vol. 26, Elsevier, New York, 1980.
- Rhines, P. B., Slow oscillations in an ocean of varying depth, 1, Abrupt topography, *J. Fluid Mech.*, 37, 161-189, 1969.
- Robinson, I. S., Tidal vorticity and residual circulation, *Deep Sea Res.*, 28, 195-212, 1981.
- Rose, K. E., Characteristics of ice flow in Marie Byrd Land, Antarctica, *J. Glaciol.*, 24, 63-75, 1979.
- Schwiderski, E. W., On charting global ocean tides, *Rev. Geophys. Space Phys.*, 18, 243-268, 1980a.
- Schwiderski, E. W., Global ocean tides, 2, The semidiurnal principal lunar tide (M2), Atlas of tidal charts and maps, *Tech. Rep. 79-414*, Naval Surface Weapons Center, Dahlgren, Va., 1980b.
- Schwiderski, E. W., Global ocean tides, 3, The semidiurnal principal solar tide (S2), Atlas of tidal charts and maps, *Tech. Rep. 81-122*, Naval Surface Weapons Center, Dahlgren, Va., 1981a.
- Schwiderski, E. W., Global ocean tides, 4, The diurnal luni-solar declinational tide (K1), Atlas of tidal charts and maps, *Tech. Rep. 81-142*, Naval Surface Weapons Center, Dahlgren, Va., 1981b.
- Schwiderski, E. W., Global ocean tides, 5, The diurnal principal lunar tide (O1), Atlas of tidal charts and maps, *Tech. Rep. 81-144*, Naval Surface Weapons Center, Dahlgren, Va., 1981c.
- Schwiderski, E. W., Global ocean tides, 6, The semidiurnal elliptical lunar tide (N2), Atlas of tidal charts and maps, *Tech. Rep. 81-218*, Naval Surface Weapons Center, Dahlgren, Va., 1981d.
- Schwiderski, E. W., Global ocean tides, 7, The diurnal principal solar tide (P1), Atlas of tidal charts and maps, *Tech. Rep. 81-220*, Naval Surface Weapons Center, Dahlgren, Va., 1981e.
- Simpson, J. H., and R. D. Pingree, Shallow sea fronts produced by tidal stirring, in *Oceanic Fronts in Coastal Processes*, edited by M. J. Bowman and W. E. Esaias, pp. 29-42, Springer-Verlag, New York, 1977.
- Thiel, E. C., Tides on the Ross Ice Shelf, *J. Geophys. Res.*, 65, 2561-2562, 1960.
- Thiel, E. C., A. P. Crary, R. A. Haubrich, and J. C. Behrendt, Gravitic determination of ocean tide, Weddell and Ross Seas, Antarctica, *J. Geophys. Res.*, 65, 629-636, 1960.
- Thomas, R. H., and C. R. Bentley, The equilibrium state of the eastern half of the Ross Ice Shelf, *J. Glaciol.*, 20, 509-518, 1978.
- Thomson, R. E., and W. R. Crawford, The generation of diurnal period shelf waves by tidal currents, *J. Phys. Oceanogr.*, 12, 635-643, 1982.
- Truesdale, R. S., and T. B. Kellogg, Ross Sea diatoms: Modern assemblage distributions and their relationship to ecologic, oceanographic, and sedimentary conditions, *Mar. Micropaleontol.*, 4, 13-31, 1979.
- Williams, R. T., The Ocean Tide Beneath the Ross Ice Shelf, Master of Science Thesis, Virg. Polytech. Inst. and State Univ., Blacksburg, Va., 1976.
- Williams, R. T., The Ocean Tide Beneath the Ross Ice Shelf, Antarctica, Ph.D. thesis, Virg. Polytech. Inst. and State Univ., Blacksburg, Va., 1979.
- Williams, R. T., and E. S. Robinson, Ocean tide and waves beneath the Ross Ice Shelf, Antarctica, *Science*, 203, 443-445, 1979.
- Williams, R. T., and E. S. Robinson, The ocean tide in the southern Ross Sea, *J. Geophys. Res.*, 85, 6689-6696, 1980.
- Williams, R. T., and E. S. Robinson, Flexural waves in the Ross Ice Shelf, *J. Geophys. Res.*, 86, 6643-6648, 1981.
- Zimmerman, J. T. F., Dynamics, diffusion and geomorphological significance of tidal residual eddies, *Nature*, 290, 549-555, 1981.

D. R. MacAyeal, Department of the Geophysical Sciences, The University of Chicago, 5734 South Ellis Avenue, Chicago, IL 60637.

(Received September 30, 1982;  
revised June 20, 1983;  
accepted August 22, 1983.)